

Complex patterns of multiple diffusive source areas for high-frequency volcanic tremor on Mt. Etna

Maurice Weber *1, Christopher J. Bean 1, Jean Baptiste Tary 1, Jean Soubestre 2,3, Ivan Lokmer 4, Silvio De Angelis 5,6, Luciano Zuccarello 6,5, Patrick Smith 1
*Corresponding author

- 1 Dublin Institute for Advanced Studies, Dublin, Ireland
- 2 ISTerre, CNRS, IRD, Université Grenoble Alpes, Université Savoie Mont Blanc, Université Gustave Eiffel, Grenoble, France
- 3 Icelandic Meteorological Office, Reykjavik, Iceland
- 4 University College Dublin, Dublin, Ireland
- 5 University of Liverpool, Liverpool, UK
- 6 Istituto Nazionale di Geofisica e Vulcanologia, Sezione di Pisa, Pisa, Italy

Complex patterns of multiple diffusive source areas for high-frequency volcanic tremor on Mt. Etna

Maurice Weber¹, Christopher J. Bean¹, Jean Baptiste Tary¹, Jean Soubestre^{2,3}, Ivan Lokmer⁴, Silvio De Angelis^{5,6}, Luciano Zuccarello^{6,5}, Patrick Smith¹

¹Dublin Institute for Advanced Studies, Dublin, Ireland
²ISTerre, CNRS, IRD, Université Grenoble Alpes, Université Savoie Mont Blanc, Université Gustave Eiffel, Grenoble, France
³Icelandic Meteorological Office, Reykjavik, Iceland
⁴University College Dublin, Dublin, Ireland
⁵University of Liverpool, Liverpool, UK
⁶Istituto Nazionale di Geofisica e Vulcanologia, Sezione di Pisa, Pisa, Italy

Received 2025 October 18

SUMMARY

In this study we present results from an unprecedented, dense, high-resolution seismic deployment on Mt. Etna that reveal rarely observed high-frequency tremor, predominantly in the $12{\text -}15Hz$ band. Such signals are typically overlooked at volcanoes due to strong scattering and rapid attenuation, which restrict their detection to near-source regions. By combining multi-array beamforming with a three-dimensional grid search based on shifted and stacked cross-correlation functions, we identify three principal tremor source regions across the summit. The most persistent source coincides with degassing activity at Bocca Nuova Crater (BNC), where synthetic tests constrain tremor and impulsive degassing events to shallow depths ($\sim 270{\text -}470m$). Temporal changes in apparent slowness further indicate alternating downward and upward propagating tremor sources beneath BNC.

In addition, two further source regions are detected to the southwest and northwest of BNC. As no degassing is known in these areas, a direct fluid-driven relationship is not expected. Instead, the spatially diffuse character of these sources, suggests these tremor episodes may be the result of numerous low-amplitude, small stress-drop events closely spaced in time and thus appearing as tremor. This hypothesis is in agreement with previous numerical and laboratory studies associating volcanic tremor with quasi-brittle failure of the weak volcanic material unrelated to fluid migration, but linked to small stress level changes driven by slow deformation of the edifice. We carry out synthetic tests showing the successful recovery of multiple superimposed tremor sources embedded in strong noise despite imperfect station coverage.

Our findings highlight the diversity of processes generating high-frequency volcanic tremor. Furthermore, we detect a temporal correlation between the different source regions in terms of intensifying and subsiding activity, which may be indicative of interconnected shallow tremor source regions. These results emphasize the complexity of volcanic tremor generation and underline the importance of high-resolution seismic networks for improving our understanding of the origin of volcanic tremor.

Key words: volcanic tremor – high frequencies – localisation – diffusive sources – driving mechanisms.

1 INTRODUCTION

In volcano monitoring, seismic tremor plays an important role as the highly complex signals may be driven by various processes Konstantinou & Schlindwein (2002), and thus carry valuable information on the volcano's state regarding hazard assessment. In fact, real-time monitoring of volcanic tremor may be one of the most promising tools in the quest of eruption forecasting as demonstrated by Chardot et al. (2015). A key aspect of investigating volcanic

tremor is constraining its source location, which is a challenging task due to the complexity of the signals lacking clear phase arrivals used in traditional localisation approaches (Permana et al., 2019; Leva et al., 2022). While spatial tracking of tremor sources is pivotal in volcano monitoring, identifying source locations for volcanic tremor may also help in better understanding processes involved in generating tremor-like signals.

Volcanic tremor is traditionally attributed to fluid-related processes such as magma movement or oscillation of gas-filled structures

2 Maurice Weber et al.

(Steinberg & Steinberg, 1975; Neuberg & Pointer, 2000; Williams-Jones et al., 2001; Konstantinou & Schlindwein, 2002; Salerno et al., 2018). Several studies locating tremor support this. Yukutake et al. (2017) suggest that volcanic tremor observed at Hakone volcano in Japan may be due to gas slug bursting, based on location of the tremor signals and time delays between seismic and acoustic arrivals. In another example, Grazia et al. (2006) link a change in located tremor source regions with the beginning of an effusively eruptive phase at Mount Etna, Italy. Furthermore, Almendros et al. (2014) indicate that degassing activity contributes to tremor signals recorded by locating it within the shallowest part of the plumbing system of Arenal volcano, Costa Rica. Similarly, backazimuths and slowness values obtained from Brava and Fogo islands utilising beamforming analysis point towards deeper sources than previously assumed hydrothermal processes at very shallow depth (Leva et al., 2022).

However, in contrast to these widely accepted models, several other studies propose that volcanic tremor may be produced entirely without fluids present but instead through quasi-brittle failure of very weak material that commonly constitutes volcanic edifices (Bean et al., 2013; Rowley et al., 2021). The authors conduct both numerical and laboratory tests suggesting that deformation-driven, dry mechanical failure needs to be considered as a possible source mechanism for volcanic tremor signals. This is in good agreement with numerical modelling by Amitrano (2003) who recovers diffusive failure patterns for low-stiffness material typical for volcanic edifices, showing numerous small seismic events associated with very small stress drops essentially merging into tremor. This phenomenon of individual events merging into tremor has been reported on before, e.g. by Dmitrieva et al. (2013) investigating individual events occurring in rapid succession generating a tremorlike seismic signature.

While tremor associated with bursting gas bubbles as investigated by Yukutake et al. (2017) is found at a vent's location, volcanic tremor that would be produced under the above-mentioned non-fluid related conditions would likely appear somewhat diffusive rather than localised and not necessarily confined to a degassing crater. Furthermore, if tremor is the result of small-scale brittle failure, such a process would be expected to radiate high frequencies. Therefore, in this study, we attempt to investigate this hypothesis for tremor generation closely, by locating rarely observed high-frequency tremor above $10\,Hz$ from the summit region of Mt. Etna, Sicily, Italy, recorded in summer 2022.

2 DATA

In order to target such high frequency ranges a dense high-resolution station configuration is required. McNutt (1992) reports volcanic tremor usually dominates between 10 s and 10 Hz while frequencies above are hardly ever considered. There are few exceptions such as Heleno et al. (2006). The strong attenuation exhibited by these high frequencies (Ibanez et al., 2019) means that signals can only be picked up if stations are available in very close proximity to the source.

We acquired data for this study during 2 campaigns in July and late August/early September 2022 that were carried out within the European IMPROVE Horizon 2020 and SINFONIA projects. As part of the first campaign, we installed a profile consisting of seven broadband stations (Nanometrics Trillium Compact, 120s, stations BB05-BB11), three of which included an acoustic component (Chaparral Physics, 60-UHP) and four 60s guralp broadband

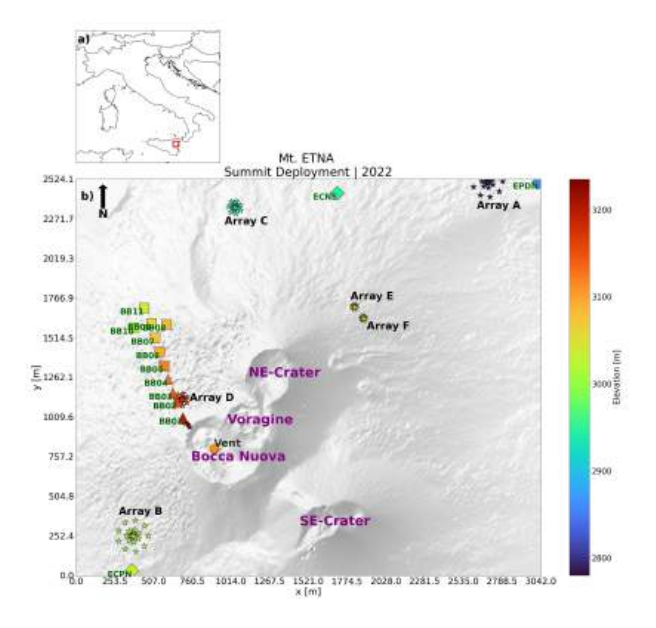


Figure 1. Study area of Mt. Etna on Sicily, Italy, marked by red rectangle (panel a)). Panel b) shows all stations deployed during data acquisition including ECPN, ECNE and EPDN which are part of the permanent network of INGV. A profile of 11 stations consisting of 7 infrasound stations as well as 4 broadband seismometers was installed alongside 6 circular array configurations (A-F) using short-period seismometers.

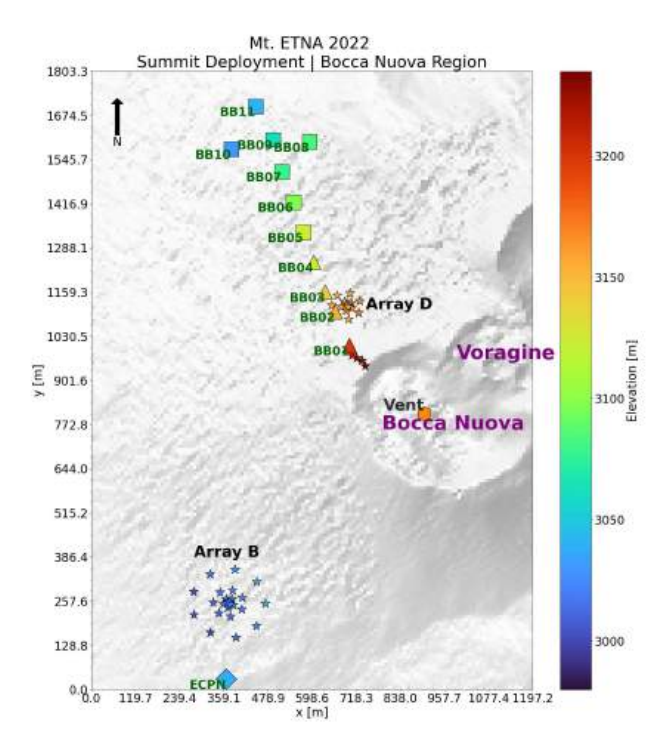


Figure 2. Zooming into the area around BNC covering Arrays B and D as well as the profile and the short-period seismometers closing the gap to the rim of BNC. Additionally, data from the INGV permanent station ECPN is used. The degassing vent's position in BNC is also marked.

seismometers (BB01-BB04) all sampling at 100 Hz (see figure 1). These remained operational for 50 days. Before the end of this acquisition, we returned for the second campaign on 25th August deploying 104 short-period seismometers (SMARTSOLO nodes) sampling at 250 Hz in circular array configurations at 6 different locations (Arrays A-F) across Mt. Etna's summit (see figure 1) recording until 1st September. This deployment was unprecedented in terms of its size, its coverage of Mt. Etna's summit area and spatial resolution capabilities. The arrays cover apertures of 30 m (2 rings with radius of 5 and 15 m, respectively, 80 m adding a third ring of 40 m radius, and 200 m adding a fourth ring with 100 mradius. The large range of inter-station distances achieved by these configurations as well as the high sampling rate tuned the arrays to be sensitive to frequencies < 5Hz (which marks the cut-off frequency where the short-period instrument's (nodal seismometers) response falls off) up to 100Hz.

The smallest arrays contain 9 stations, the medium-aperture arrays consist of 16, while the large arrays consist of 25 stations. The remaining 4 short-period instruments which were not part of any of the arrays were instead used to close the gap between the end of the profile (BB01) and the rim of the Bocca Nuova Crater (BNC). Furthermore, data from stations ECPN, ECNE and EPDN (see figure 1) from the permanent network run by the Istituto Nazionale di Geofisica e Vulcanologia (INGV) were added in order to locate volcanic tremor. The area of main interest is around BNC for which a zoomed in view is found in figure 2.

3 LOCALISATION TECHNIQUES SUITABLE FOR VOLCANIC TREMOR

As alluded to earlier, localisation of volcanic tremor is challenging due to the lack of distinguishable phase arrivals and strong scattering as a result of the extreme heterogenous conditions dominating volcanic environments. Some studies such as Almendros et al. (2014) or Leva et al. (2022) demonstrate how beamforming techniques using several array configurations can be promising to constrain source areas, while also yielding estimations on the seismic velocities without requiring a starting velocity model. Zuccarello et al. (2022) successfully track volcanic tremor resolving vent-specific activity. In this study we are utilising a multi-array beamforming tool called RETREAT developed by Smith & Bean (2020) which performs f-k analysis to calculate backazimuth and apparent slowness. Based on this we can estimate the sources' depths through comparison with synthetic source depths. This tool has the advantage that it is capable of computing backazimuth and slowness pairs for multiple arrays simultaneously.

We test a slowness grid between 0 and $4\frac{s}{km}$ with a resolution of $0.025\frac{s}{km}$ while the azimuthal binning is set to 5° amounting to 72 azimuthal bins in total. Value pairs of backazimuth and slowness are calculated for subwindows of 2 seconds with an overlap of 50% essentially computing one value pair every second. In order to predominantly focus on coherent tremor content the relative beampower associated with each value pair can be used to remove any results below a certain threshold. We discard any results <0.25 which is equivalent to about 85% of the data.

For comparison purposes and in order to get a better understanding about how diffusive or localised the detected tremor sources are, we also located tremor sources in 3D using the open source Python package called CovSeisNet (Seydoux et al., 2016; Soubestre et al., 2018; Tong et al., 2024). Seydoux et al. (2016) divide the seismic traces into subwindows and a certain number of adjacent windows

are averaged before spectral whitening is applied to the traces. After transforming into the frequency domain, cross-spectra are calculated between all station combinations yielding the Covariance Matrix of dimensions $N \times N \times f \times t$, where N refers to the number of stations, f to frequency and t to time, respectively. The cross-spectra are calculated on individual subwindows while the Covariance matrix represents the average of all cross-spectra for a certain number of consecutive subwindows. This detects coherent signal (considered to be tremor) emerging from what is uncorrelated background noise through a parameter called spectral width, defined as the width of the covariance matrix eigenvalues distribution (Seydoux et al., 2016). Subsequently, Soubestre et al. (2018) decompose the obtained covariance matrix into its eigenvectors, where the first eigenvector represents the dominant tremor source and further eigenvectors correspond to additional sources if existent until eventually eigenvectors carry uncorrelated noise only.

A 3D grid search is performed testing every grid point as a possible source by shifting the envelopes of cross-correlation functions (CCFs) between all combinations of stations according to travel times corresponding to a given velocity model (Soubestre et al., 2019). Here, travel times are calculated using NonLinLoc (Lomax et al., 2000, 2014). Travel times are based on a combined velocity model after Zuccarello et al. (2016) for the top 130 m at Pozzo Pitarrone, while the velocity structure below is taken from Trovato et al. (2014) down to 1500 m depth. While both velocity models are 1D, we generate a pseudo 3D model by taking into account the significant topography changes across the grid space using the elevation model after Ganci et al. (2023). At each grid point the 1D velocity structure starts at the respective altitude according to the topography model essentially creating a 3D velocity distribution with lateral velocity changes. A grid point close to the true source aligns all CCFs at 0s lag time producing the largest stack within the grid search and thus the point of largest likelihood. A 3D likelihood function is gained for all grid points. The smaller the grid space the smaller the differences in travel times for neighbouring grid points resulting in similar likelihood for the corresponding grid points and therefore introducing limitations in terms of resolution.

4 ROBUSTNESS OF ARRAY BEAMFORMING

As we are not only interested in the direction of arrival of high-frequency tremor that can be uncovered in our data set but in particular want to gain an understanding as to how diffusive or localised these tremor sources are, we first require a verification of the reliability of obtained beamforming results. This is addressed by testing the precision and accuracy with which a source can be recovered with the configuration of stations available.

4.1 Confirming degassing vent's location

The array beamforming's precision and accuracy can be estimated very effectively using the impulsive seismic events related to the ongoing degassing activity from BNC. The advantage here is that we know the events' origin at the vent in BNC. From Google Earth images we can constrain the vent's location very well, however, there were 2 pit-like vents seen within BNC at less than $50\ m$ from one another at the time of deployment. Only one of these vents was degassing, which we confirmed utilising the acoustic arrival time delays between 3 different infrasound stations in the linear array.

4 Maurice Weber et al.

These time delays correspond to a line of possible source points which crosses one of the 2 vent locations according to Google Earth images confirming the degassing vent's location.

4.2 Locating impulsive degassing events

We now select 30 impulsive degassing events with high S/R for which beamforming is performed using the RETREAT tool (Smith & Bean, 2020). One example event is seen in figure 3. We verify the degassing nature of the event by comparing the seismic and acoustic signature within the same 3s window showing a delay between seismic and acoustic onsets due to slower acoustic wave speed and different source-station distances (see different onsets in panels a) and b)). All data is filtered between 2-8Hz where energy was strongest and the response of the short-period instruments sufficient. Panel a) shows the seismic waveforms at central stations D01 and B01. The large difference in distance to the vent in BNC is clearly seen in the much more impulsive and earlier onset at D01. In order to determine the direction of arrival of the event's energy we focus on the onset of the event only, as the event's coda is affected by an increasing amount of scattering due to path effects. 0.75s of manually defined data is selected around the onset of the event at Array D (station D01) from which the mean apparent backazimuth and slowness are computed. Because the backazimuth-slowness pairs are calculated in 1-second subwindows with 90% overlap (to achieve very high temporal resolution), the time range used to compute the mean must begin slightly before the coherent onset at station D01 (see panel a)). As shown in panel b) of figure 3, the apparent backazimuths for Array D (bright green stars) become much more stable once the event's coherent energy dominates the calculation. This stable behavior starts exactly at the position of the dashed black line, which is why the averaging window begins there. The end of the range is set just before the apparent backazimuths grow unstable again, when the scattered coda increasingly affects the waveform.

The stable result can be attributed to the coherent energy as the event passes through the arrays suggesting a high level of precision as the values do not vary. Noticeably though, the recovered apparent backazimuths, while stable, do not point back to the vent (pink dashed line) but, instead, show a 17° difference. We find the slownesses largely align when coherent signal content is present at both arrays (see panel d) between 0.75s and 1s) while they start to deviate significantly once increasing scattering and noise take over. The backazimuth-slownesses pairs are apparent values only, as the beamforming assumes a 2D plane when, in fact, significant topography dominates the area and event origins are at different elevations than the receivers. The fact that apparent slownesses do not align perfectly for Arrays D and B during the time of coherent signal content is expected due to the difference in elevation between the 2 arrays - Array D is situated at an elevation about 100 m higher resulting in slightly different apparent slownesses relative to the event's source elevation, compared to Array B. The increasing apparent slownesses during the period of coherent signal for both Arrays B and D implies a rising source which is consistent with the assumption that this event is caused by impulsive degassing.

The same procedure is carried out for a selection of 29 other events yielding 30 mean apparent backazimuth and slowness pairs. An overview of how they distribute is shown in figure 4. We find most of the backazimuths clustering around a similar direction of arrival as the individual event presented in figure 3 with a few located around the southern rim of BNC and only 2 nearby the vent's location. As the beamforming assumes a 2D plane varying slownesses

are likely indicative of different source depths as deeper sources translate to higher apparent velocities and thus a smaller apparent slowness. These results are next compared to synthetic event tests to examine if the observed offsets between the vent and the recovered apparent backazimuths are due to limited accuracy or the use of apparent slownesses (due to 2D plane assumption), which can be inverted for event source elevations.

4.3 Synthetic event recovery and depth estimation of impulsive degassing events

We generate multiple events at varying depth using the NonLinLoc package (Lomax et al., 2000, 2014) to calculate travel times based on a combined P-wave velocity model after Zuccarello et al. (2016) for the top $130\ m$ at Pozzo Pitarrone while the velocity structure below is taken from Trovato et al. (2014) down to $1500\ m$ depth. The waveforms at the corresponding arrival time at the various stations are generated using a Ricker wavelet with dominant frequency at $4\ Hz$ as observed for the real events. Additionally, significant random noise is added to the traces producing realistic S/R (ratio of 3) similar or worse than what is observed in the real data set. The synthetic events are placed at the confirmed vent's location; one at the surface and $10\ m$ further events at $100\ m$ increments down to $1\ km$ below the surface.

For the synthetic event in figure 5 at 2970 m elevation (300 mdepth) we find a stable apparent backazimuth at an almost identical mean value as observed for the real event discussed in figure 3 (165.6° vs 167.5° for Array D). Similarly, for the apparent slownesses we find an almost identical mean as well $(0.72 \frac{km}{s})$ vs $0.78\frac{km}{2}$). Also, both the overall means for apparent backazimuths (166.9°) and slownesses $(0.83 \frac{km}{s})$ for all 30 real events tested show only negligible differences to this synthetic result. Therefore, we assume the average source elevation can roughly be expected at 3000 m a.s.l (250-300m depths). Furthermore, the synthetic tests show that once the calculation subwindow moves away from the coherent waveforms, the analysed signal is dominated by path effects and both apparent backazimuth and slowness estimations become unstable. This agrees with previous assumptions about the real event (figure 3). The elevation difference between Arrays B and D results in slightly smaller apparent slownesses for the latter because of its higher elevation.

When plotting all synthetic event results together (see bottom panel in figure 6) we find a clear dependency on the source elevation as apparent slownesses increase significantly between roughly 3000 and 3100 m a.s.l. This depth-dependent behaviour is expected due to the beamforming assuming a 2D plane. Based on the synthetic and real slownesses observed we ultimately constrain the likely source elevations for the degassing events at 2800 to 3000 m a.s.l. (270-470m depth) as the discrepancy between synthetic slownesses and those found for real events extends significantly beyond one standard deviation for the range of real slownesses at lower or higher elevations.

The same depth-dependency is observed for the apparent backazimuths as well (panel a)) where only very-near-surface events are located correctly at the vent. The synthetic event at the surface is recovered with excellent precision as the direction of arrival points back exactly to the vent's location (similar to resolution capabilities reported by Zuccarello et al. (2022)). Events at 2800-3000m a.s.l. are found closer to the southern rim where most of the real events are located. Larger apparent backazimuths are obtained for larger synthetic source depths (i.e., lower source elevations). Therefore, we can explain the average backazimuth pointing back

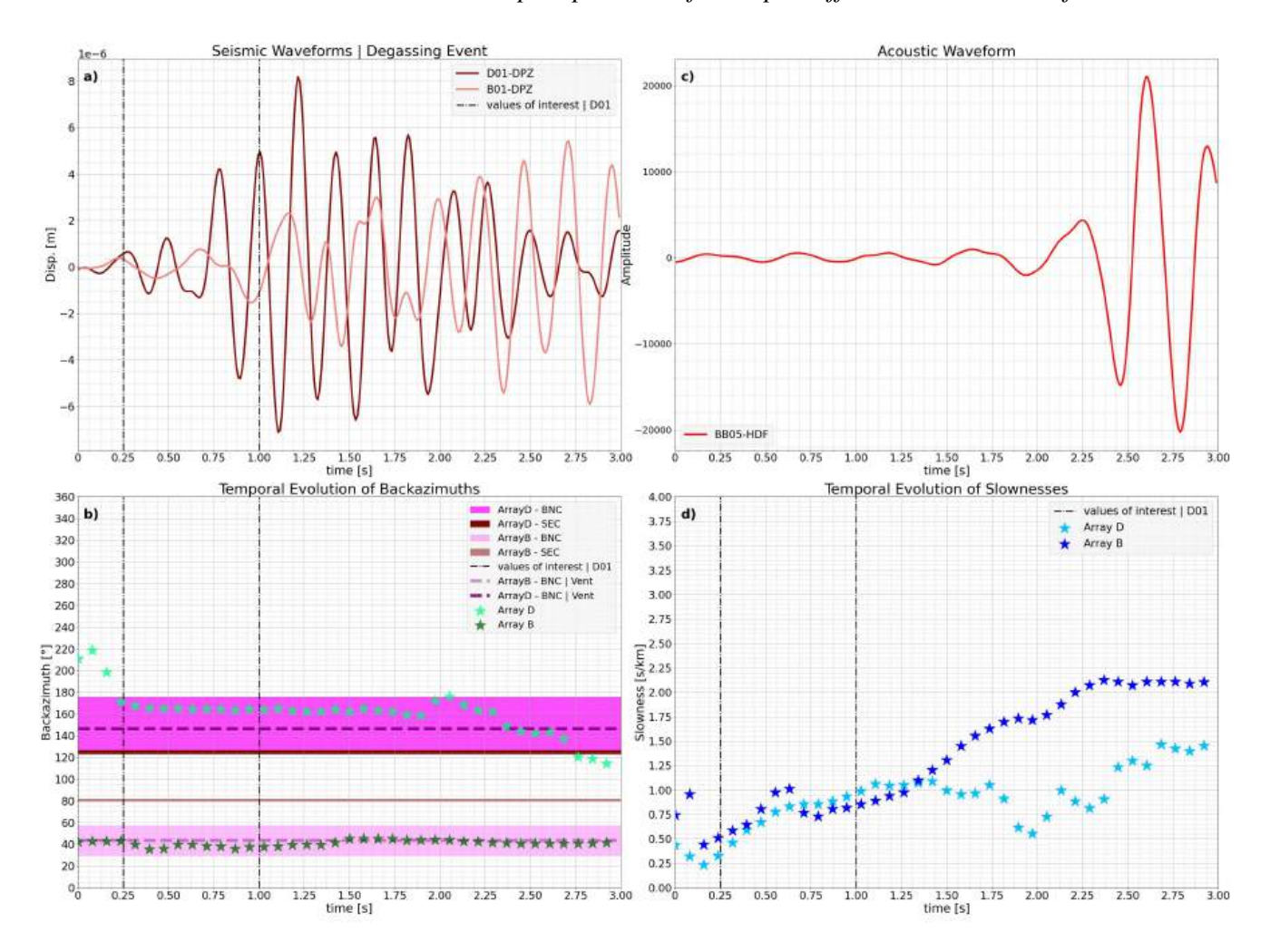


Figure 3. Beamforming carried out for a high-quality impulsive degassing event. Panel a) shows the waveforms for central stations of Arrays B and D (B01 and D01) filtered between 2-8 Hz around the onset of the event. Both stations feature a different distance to the vent in BNC (378 and 798 m, respectively). In panel c) the corresponding acoustic waveform for the infrasound station closest to the vent (BB05) is displayed confirming that this event was indeed a degassing event. All panels and traces start at the same time. In panel b) the temporal evolution of the apparent backazimuth values during the event is shown for both arrays. Additionally, highlighted in bright pink is the range of apparent backazimuths covering the BNC seen from Arrays B and D, respectively, while the dark pink line marks the direction towards the vent seen from both Arrays. The same is done for the South Est Crater (SEC). The dashed black vertical lines mark the manually defined time window from which apparent backazimuths are selected to compute the mean direction of arrival for this event focusing on the coherent onset for Array D only. Finally, in panel d) the temporal evolution of the corresponding apparent slownesses are found, once again for both Arrays B and D where the mean slowness for Array D is calculated from the same selected range (black dashed lines).

closer to the southern rim than to the vent's location as an effect of geometry: For 2D beamforming, backazimuths will be estimated correctly only for sources located in the same plane as the arrays. On the other hand, as the sources move deeper, timings will change differently depending on the relative positions between sources and arrays. For example, travel times become much larger for Array D than for Array B as sources move deeper, leading to travel times that are increasingly similar. To account for this a direction of arrival closer towards a point with similar distance to both arrays is found. This condition is met for backazimuths closer to the southern rim of BNC rather than the vent seen from Array D which is why most events are located towards this direction. From Array B's point of view directions of arrival are almost unaffected as these backazimuths are still aligned with the vent (figure 3).

Subsequently, we assume that the offset observed between the mean backazimuth for the real events tested and the vent's loca-

tion is largely due to the 2D beamforming, and is not a sign of beamforming inaccuracy. In fact, a synthetic event generated at the surface at the vent's location is recovered with excellent precision. The systematic offset in backazimuths obtained for Array D will need to be taken into account when analysing source areas of high-frequency tremor.

5 ARRAY-BASED SPATIAL AND TEMPORAL TRACKING OF HIGH FREQUENCY TREMOR THROUGH BEAMFORMING

We find high-frequency tremor episodes dominating mainly in the 12-15Hz band throughout the week-long deployment of the 104 short-period instruments (see figure 7). For example, a clearly visible high-frequency tremor episode is found between 16:00

6 Maurice Weber et al.

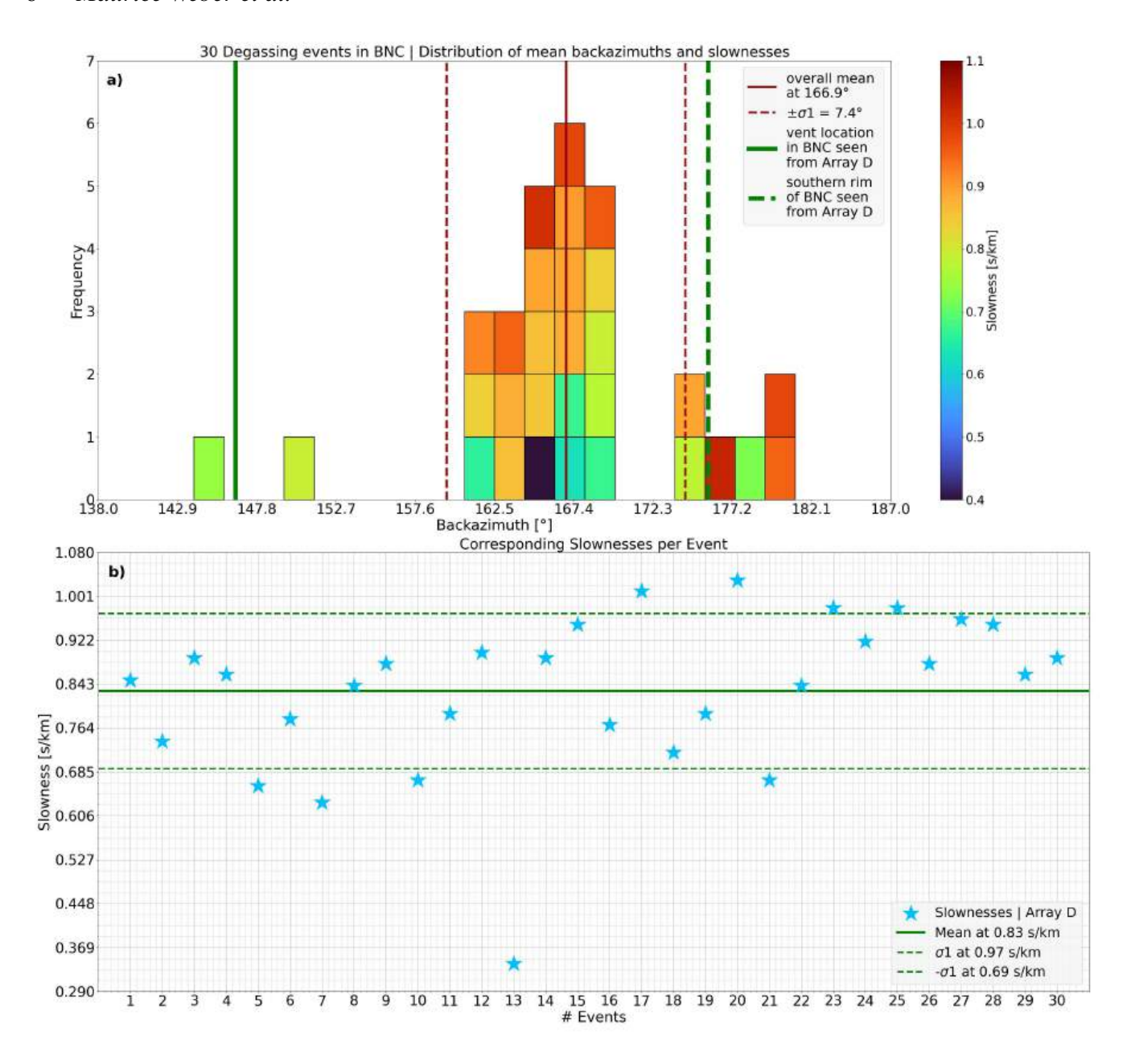


Figure 4. Recovered apparent backazimuth and slowness pairs for all 30 events tested. They are colour-coded with respect to the corresponding slowness in panel a). Additional vertical lines show the direction towards the vent seen from Array D as well as the southern rim of BNC for orientation. The overall mean and standard deviations of the apparent backazimuths are indicated as well. Panel b includes all slownesses for the respective events and their overall mean and standard deviations.

and 17:00 UTC on 30th August, lasting about 30 minutes. High-frequency tremor also re-emerges at later times. As mentioned earlier, such frequency ranges have been rarely considered on Mount Etna with exceptions like Cannata et al. (2010) which is partly due to their rapid attenuation, the strong scattering exhibited at frequencies above 10Hz (Ibanez et al., 2019) and the volcano's typical ever-present tremor bands covering frequencies between 2s-5Hz as reported by Lieto et al. (2007) (also seen constantly in figure 7) that are therefore traditionally used for monitoring purposes while higher frequencies are simply overlooked. We thus focus on these poorly understood frequency ranges with the opening question as

to whether these high-frequency signals can be generated by failure of weak material in the volcano's edifice.

5.1 Revealing multiple larger source areas of volcanic tremor

In order to best visualise the evolution of recorded tremor in both time and space, we plot backazimuth and apparent slowness as a function of time for Arrays B and D (figures 1 and 2) filtering in the target range of 12-15 Hz. A total of 20 hours of data between 25th August 2022, 16:00 UTC and 26th August 2022, 12:00 UTC are shown in figure 8. While beamforming is computed for both arrays B and D simultaneously, only the results for Array D are

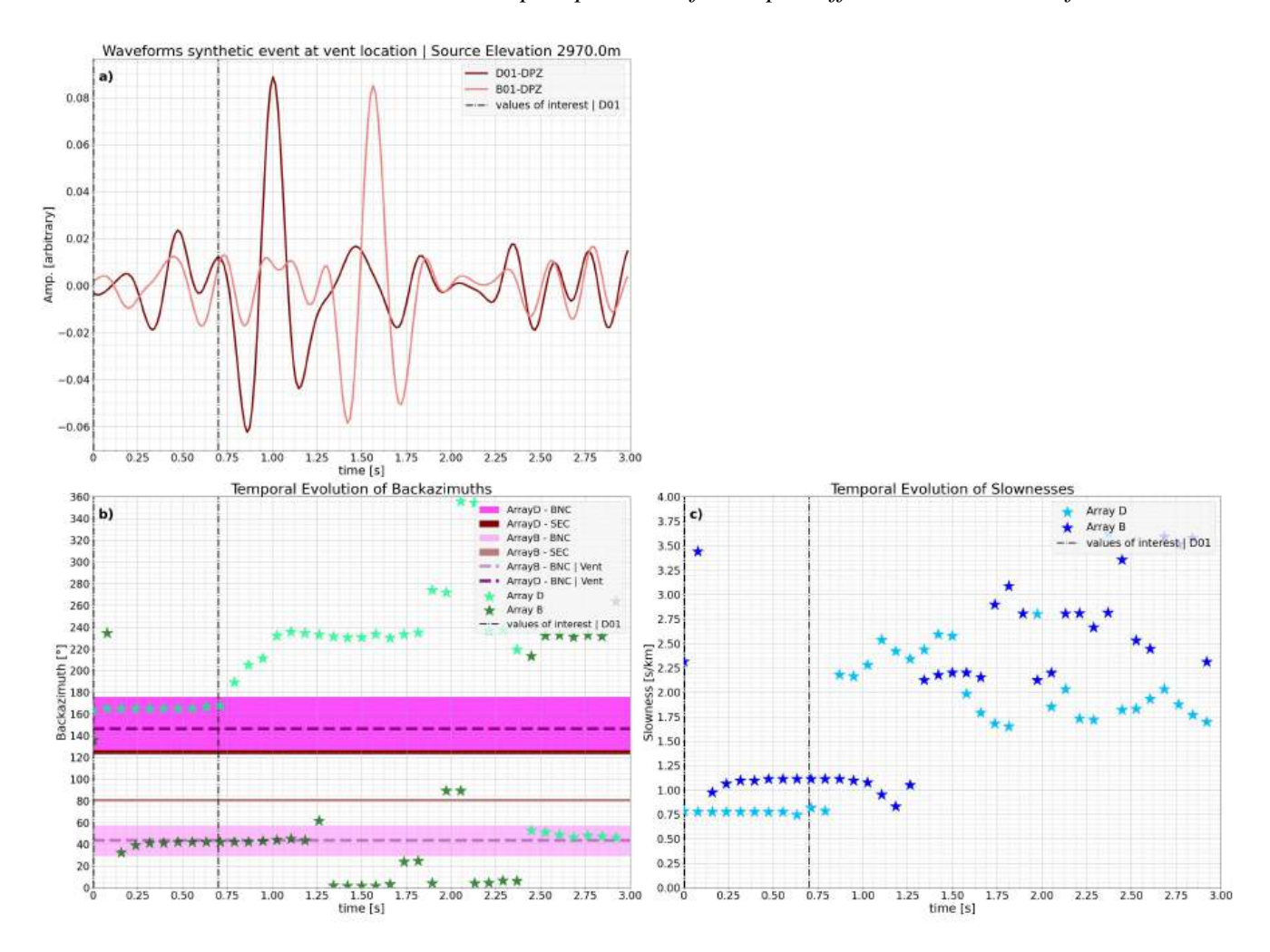


Figure 5. Similar to figure 3 waveforms, apparent backazimuths and slownesses are displayed for one of the synthetic events generated at the vent's location in BNC at an elevation of 2970 m (300 m depth).

shown here as this array is best located to show directional variations for incoming tremor. Arrays A, C, E and F are largely too far away to pick up the same signals as Array D and B in the rapidly attenuating frequencies > 10Hz. The apparent backazimuth and slowness pairs are directly compared to the average seismic amplitude from all stations in Array D (panel a) in figure 8).

Firstly, we find a significant variability over time shown by the seismic energy output hinting at variable activity of the volcano. There was no eruptive activity occurring at the time of the deployment, yet even in a state of apparent quiescence the summit region of Mount Etna produces a broad spectrum of seismic output. The most dominant source of the recorded high-frequency seismic energy is radiated from BNC where most of the obtained apparent backazimuths are clustered (panel b) in figure 8). However, the direction of arrival (from Array D's point of view) clearly points the southern half of BNC covering the range between the vent's location (purple solid thin line) and the southern rim at about 180° matching the same range observed for the 30 impulsive degassing events in figure 4. Also note, how the associated apparent slownesses range from about $0.4-1.5\frac{s}{km}$ within the BNC area which is also in good agreement with what was observed for the degassing events, suggesting that the tremor produced in BNC originates from a similar range of depth as the discrete seismic events ($\sim 270-470m$). Moreover, we observe a decreasing trend in apparent slownesses from $1.5 \frac{s}{km}$ at the vent to $0.4 \frac{s}{km}$ around the southern rim of BNC. Based on the earlier findings on depth-dependent variations of apparent backazimuth and slowness we conclude that most of the blue colour-coded backazimuths in the southern half of BNC and those slightly south of it are largely artificially shifted to those locations as a consequence of 2D beamforming and out-of-plane sources. Instead, the true locations are expected to be mostly confined to the vent's immediate vicinity where apparent backazimuths corresponding to a higher slowness (>1.0 \frac{s}{km}) are found. They are likely originating from sources at shallow depths (> 3000ma.s.l., < 170m depth), for which directional characteristics are estimated more accurately as the source-receiver geometry is closer to a 2D plane (synthetic tests showed an expected apparent slowness of $\sim 1.7 \frac{s}{km}$ for an event generated at the surface).

While tremor tied to the degassing vent is consistent with the established models relating volcanic tremor to degassing activity, our results here reveal two main additional tremor sources off the summit craters where tremor is not commonly found and no degassing activity is expected to occur there. One of them covers an area roughly to the southwest of BNC between 210-240°. Noticeable are the exceptionally high apparent slownesses associated with it, ranging between about 2.8-3.7 $\frac{km}{s}$, which would translate to appar

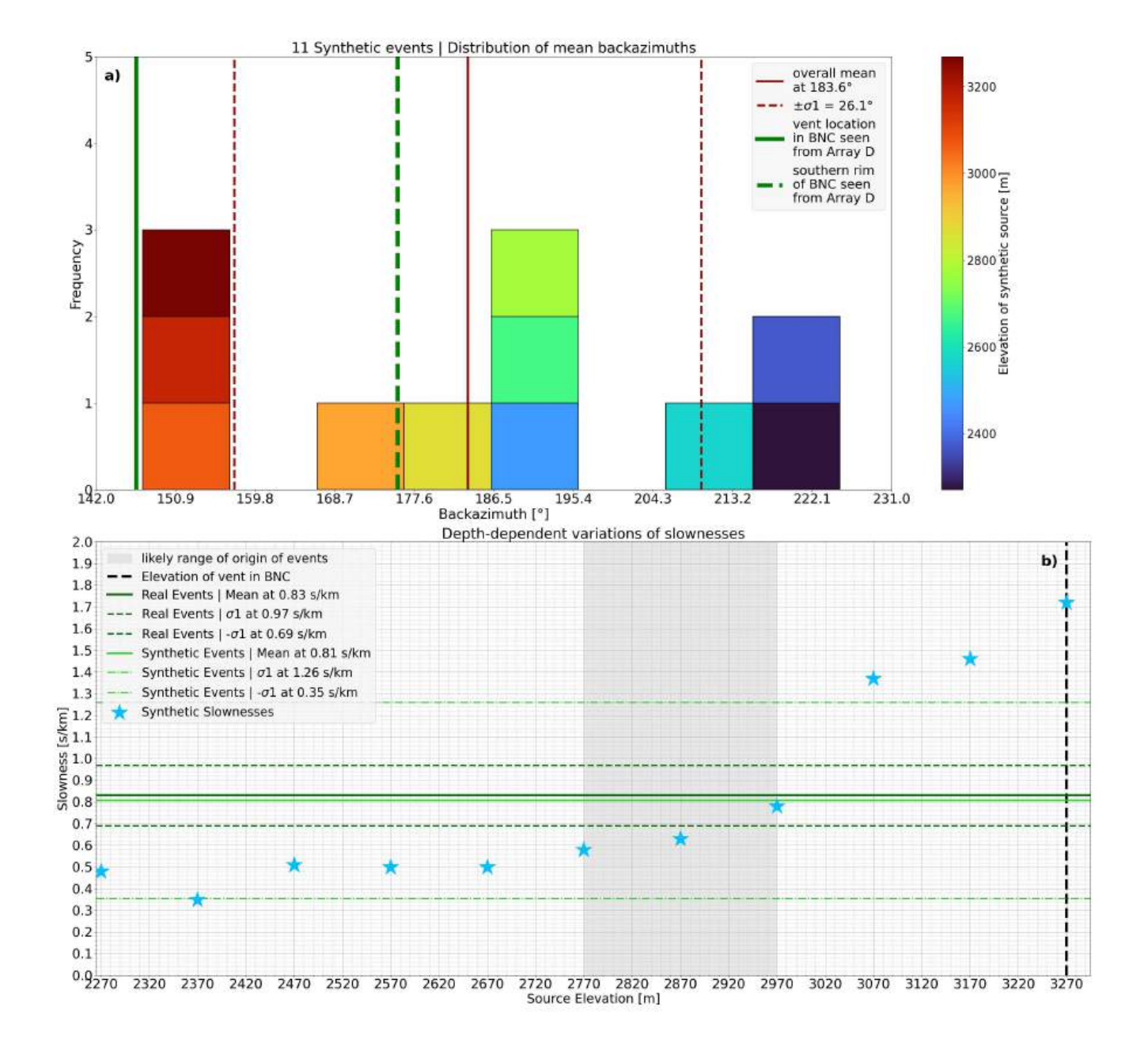


Figure 6. Distribution of synthetic apparent backazimuths (panel a)) colour-coded according to the event's source elevation and the corresponding apparent slownesses below (panel b)) as a function of the source elevation. Similar to figure 4 direction towards the vent and the southern rim of BNC as well as overall mean and standard deviations are indicated. The grey area in panel b) marks the most likely range for source elevations based on the recovered real apparent slownesses in comparison with the synthetic ones. Real slownesses are marked by the dark green lines while the bright green lines show overall mean and standard deviations for the synthetic slownesses. The black dashed vertical line indicates the surface elevation at the vent's location in BNC.

ent velocities near or even below sound speed. Zuccarello et al. (2016) finds $600\frac{m}{s}$ for Vp and $300\frac{m}{s}$ for Vs - very low velocities in the uppermost deposits of very weak material at the summit are possible. Tremor associated with this direction of arrival is likely due to very near-surface sources. The other striking observation to be made about this signal is its temporal variability - it only appears episodically and this behaviour stops at 01:00 UTC on 26th August 2022. Whenever this signal appears there are almost no directions of arrival found pointing to BNC which means that signals from this new source area dominate. Some energy may still be radiated from BNC at these times, however, it is weak enough to be

completely overshadowed by the $210\text{-}240^\circ$ source. A time zoom of one of these episodes around 01:00 UTC on 26th August 2022 indicates the tremor is propagating out of BNC (and to the surface given the large increase in apparent slowness), while activity in BNC decreases gradually. On the other hand, a far more abrupt switch back to BNC is observed within a couple of minutes shortly before 01:30 UTC.

Interestingly, the episodic appearance of this signal seems to coincide with a drop in seismic energy (panel a)). This correlation, however, is incomplete as the strongest episode of this signal found around 01:00 UTC does not appear at the time of lowest seismic



Figure 7. 8 hours of data investigated for signal coherency between all stations in Array D using the tremor detection tool COVSEISNET. Yellowish colour indicates coherent signal at given time and frequency while increasing dark colours represent dominating uncorrelated noise.

energy output. Later during this 20 hour window, the behaviour of this source changes to a more constant but less dominant appearance after about 03:00 UTC on 26th August 2022. Unlike for the episodic appearances before, BNC is the dominant source at the time. Since seismic energy decreases significantly after 03:00 UTC, we assume this source is indeed not constantly active but changes intensity over time. The earlier episodic appearance may be explained by strong activity from BNC, which usually masks the 210-240° source, except during periods when seismic energy levels drop sufficiently. If the source was of the same intensity as before we would expect this source to be much more dominant after 03:00 UTC on 26th August 2022 as the overall seismic energy output subsides. The fact that it is not suggests a decrease in intensity of this source area. Since the seismic amplitude decreases strongly after 03:00 (and in particular after 05:00 UTC on 26th August 2022) the activity from BNC is also diminishing during this period.

The third dominant direction of arrival obtained from this time window is found between 300-330° which is far off any known degassing summit craters. Similar to the previously discussed source, this one exhibits episodic behaviour before disappearing entirely after 04:00 UTC on 26th August 2022. There is a very noticeable correlation between the recorded level of seismic energy output and the appearance of this signal. Spikes in seismic amplitude coincide very well with directions of arrival from 300-330°. Since the activity from BNC is very strong at the time, this signal could arise from a reflection of the energy radiated from BNC. However, in this case, we would expect the amplitude of this signal to correlate with the level of seismic energy. This does not seem to be the case when comparing the peak just before 05:00 UTC on August 26, 2022 which is not associated with apparent backazimuths from 300-330°, while an earlier peak at 21:00 UTC on August 25, 2022, is associated with both lower levels of seismic energy and the presence of arrivals from 300-330°. We therefore assume that this signal is indeed coming from an independent source rather than being a reflection and it's appearance increases the overall seismic output at the respective times.

As mentioned earlier we are evaluating how diffusive the

tremor sources are and, interestingly, neither of the two tremor source areas outside of BNC shows a very point-focused character but are somewhat diffusive across a range of apparent backazimuths. In contrast, the tremor related to BNC activity is likely to be emerging from a very narrow range around the vent as discussed above. The high apparent slownesses (>1.5 $\frac{s}{km}$ for the 300-330° source and 2.8-3.7 $\frac{km}{s}$ for the 210-240° source) indicate a near-surface origins with sources and receivers approximately in a 2D plane. Therefore, the spatially diffusive character of these tremor sources can be considered a real feature as opposed to the BNC source associated with deeper sources (lower apparent slownesses). Furthermore, the edifice undergoes a clear transition between approximately 03:00 and 05:00 UTC on 26th August, during which all three main tremor sources exhibit significant changes in their characteristics.

We now focus on another 20 hour period between 12:00 UTC on 31st August and 08:00 UTC on 1st September, 2022, displayed in figure 9. We observe the same three main sources of high-frequency tremor we have identified before - one clearly related to the degassing activity at the vent in BNC originating largely from about 2800 to 3000 m based on the associated apparent slownesses, while the other two are not spatially linked to BNC, appear at 210-240° and 300-330°, respectively. Similar to before a significant temporal variation in the appearance and intensity of these three sources can be observed.

The first notable change in behaviour occurs between 13:00 and 15:00 UTC on 31st August, 2022, when the 210-240° source area becomes active, peaking around 14:30 UTC. At the time BNC shows a similar gradual reduction in energy output as observed in figure 8 for the episode around 01:00 UTC on 26th August, 2022. This transition of tremor activity from BNC to 210-240° lasts for over 2 hours, making it significantly more prolonged than the earlier event shown in figure 8. There is no visible change in seismic energy output registered as the 210-240° source begins to take over at around 13:00 UTC on 31st August, 2022, clearly suggesting that this source area was not previously superimposed by a stronger crater activity. Instead, the data imply a genuine propagation of tremor from BNC to the southwest (210-240° source) and towards

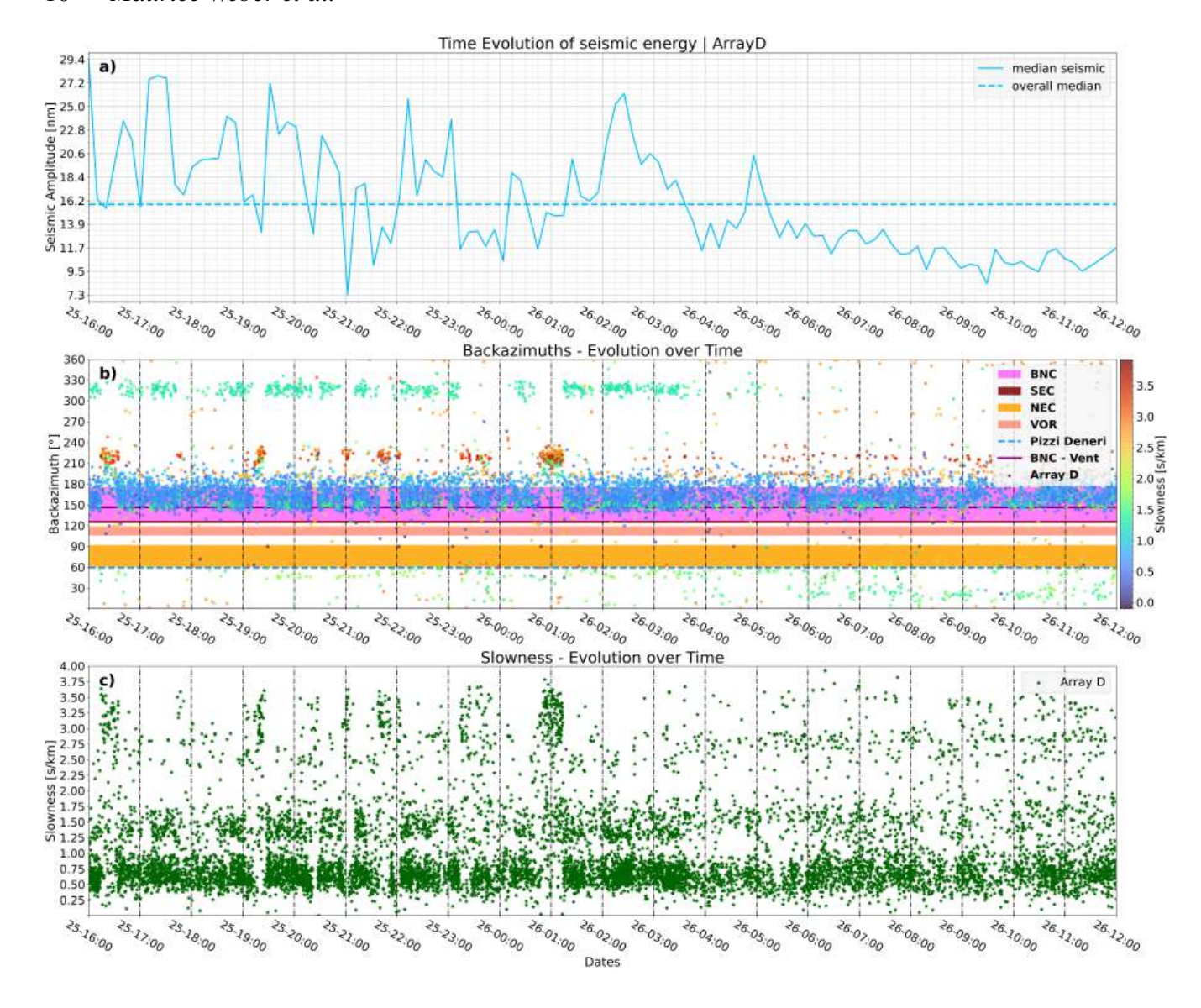


Figure 8. Evolution of median seismic amplitudes at target frequency of 12-15Hz averaged for all stations in Array D computed for 10-minute, non-overlapping windows for 20 hours between 16:00 UTC on 25th August and 12:00 UTC on 26th August (panel a)). Overall respective mean is added as a dashed horizontal line. Panel b): Temporal evolution of backazimuth for Array D. Shaded background areas in different colours refer to the azimuthal range covered by the summit craters and Pizzi Deneri Observatory seen from the array's point of view. Additionally, direction towards the vent's location in BNC is indicated. Backazimuth values are colour-coded with respect to the corresponding slowness which are shown in panel c). All backazimuth and slowness pairs pairs associated with a relative beampower < 0.25 are removed (about 85% of data) to focus on coherent signal content.

the surface considering the exceptionally high apparent slownesses encountered. This potentially suggests inter-connected source areas for high-frequency tremor on the edifice at the time.

A repeat of a similar pattern is found between 06:00 and shortly before 08:00 UTC on 1st lasting a similar duration and showing a similar gradual change where BNC activity subsides while 210-240° intensifies until shortly before 08:00 UTC on 1st September, 2022, when a very sudden return of the tremor to BNC is detected. Again, this transition is not accompanied by a clear change in seismic amplitude albeit the energy output being much higher at this time than for the first event between 13:00 and 15:00 UTC on 31st August, 2022. This reinforces the assumption that this source appears periodically and is otherwise inactive rather than being masked by a stronger crater activity. In the 5 hours preceding the second event starting at 06:00 UTC several strong peaks in seismic energy are

registered, representing the highest amplitudes of the entire deployment period. They seem to be caused by a re-appearance of the 300-330° source, although the elevated energy levels are also likely influenced by a substantial increase in activity at BNC occurring simultaneously.

While the previously identified sources of tremor originating from outside BNC show a slightly diffusive character as found before in figure 8 there are three distinct instances of a more localised signal centered around 220° that are observed between 20:00 UTC on 31 August and 00:00 UTC on 1 September, 2022. These events mark a shift toward more focused tremor activity originating from the southwest of BNC. Apparent slownesses remain very high indicating a very near-surface origin confined to a smaller area. Another noteworthy observation is the nearly cyclical variation in

apparent slowness associated with tremor emanating from BNC oc-

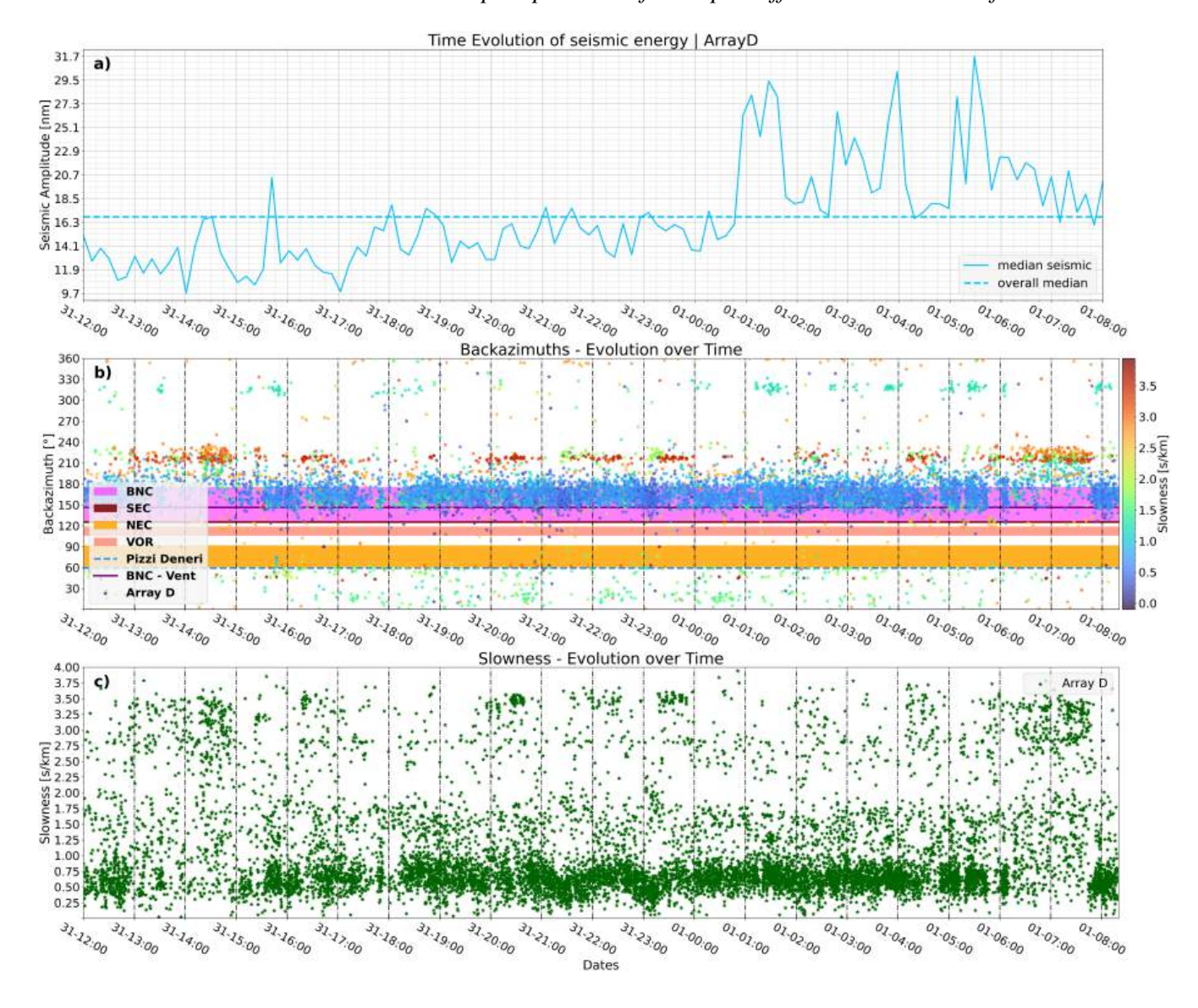


Figure 9. Temporal evolution of median seismic amplitudes (panel a)), backazimuth (panel b)) and slowness (panel c)) displayed as in figure 8 looking at 20 hours between 12:00 UTC on 31st August and 08:21 UTC on 1st September.

curring between approximately 21:00 on 31st August and 00:00 UTC on 1st September, 2022. Apparent slownesses fluctuate from 0.2 to $1.0 \frac{s}{km}$ in 2 cycles of ~ 1.5 hour periods (panels b) and c), in figure 9). This is indicative of downward and upward propagating tremor sources underneath the vent in BNC.

6 NETWORK-BASED 3D LOCALISATION OF HIGH-FREQUENCY TREMOR THROUGH BACKPROJECTION

To further investigate the source distribution of the high-frequency tremor we are using COVSEISNET to locate them in 3D (Soubestre et al., 2019; Seydoux et al., 2016; Soubestre et al., 2018). A distribution of stations that provides a good coverage across the grid space is important, however, our deployment layout on Mt. Etna was not initially intended for network-based localisation but mainly geared towards multi-array beamforming. In addition to this challenging station distribution, the localisation problem is further

complicated due to the high-frequency character of the signals and small grid space, leading to small travel-time differences between stations. As we are particularly interested in studying how spatially diffusive the high-frequency tremor sources behave, we are initially carrying out synthetic tests to evaluate how two discrete tremor sources can be recovered in terms of smearing of the obtained likelihood distribution.

6.1 Recovery of source locations of synthetic tremor composed of 2 sources

For these tests, we use a selection of 14 stations for best possible coverage which includes 3 stations from the INGV permanent network (ECPN, ECNE, EPDN, figure 1). The 2 synthetic sources are placed to the Northwest of Array D to represent the signal we observe appearing from 300-330°. Two sources are generated in relative close proximity as we are attempting to simulate a spatially diffusive source region where multiple discrete sources are active

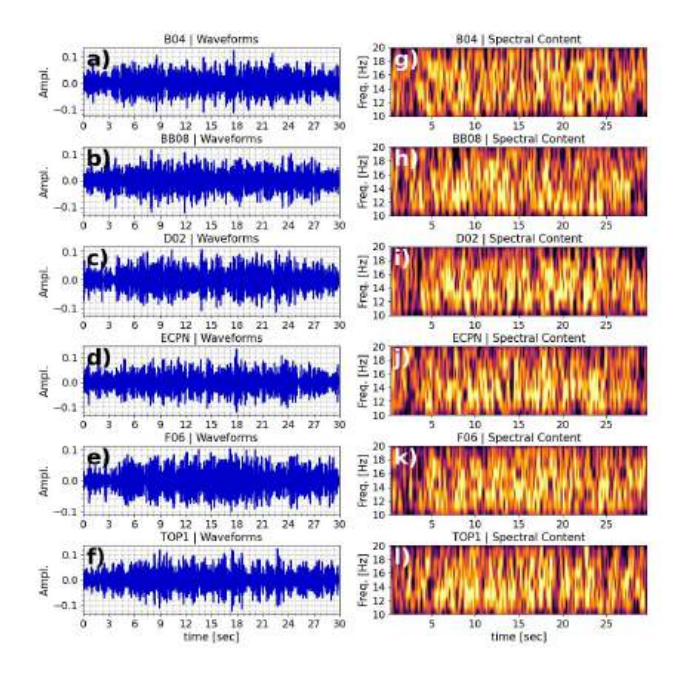


Figure 10. 30s of synthetic waveforms are shown for 6 out of 14 stations (panels a)-f)), simulating high-frequency tremor emerging from 2 distinct sources in close proximity. Tremor episodes are generated using ricker wavelets for both sources centered around 13.5~Hz matching the real data's tremor band and repeated 135 times with random offsets. Data is filtered between 10-20~Hz and both tremor episodes are superimposed. Significant normal gaussian noise is added at standard deviation of 0.05 while initial maximum signal amplitude is 0.1. Corresponding spectral contents are found in panels g)-l).

simultaneously, consistent with numerical simulations by Amitrano (2003) and Bean et al. (2013). Their studies suggest quasi-brittle failure associated with a diffusive damage pattern which may be reflected in the broad backazimuthal range of approximately 30° covered by this signal.

In order to generate the synthetic sources, Ricker wavelets are convolved with a unit impulse at timings calculated for selected stations using NonLinLoc (Lomax et al., 2000, 2014). The dominant

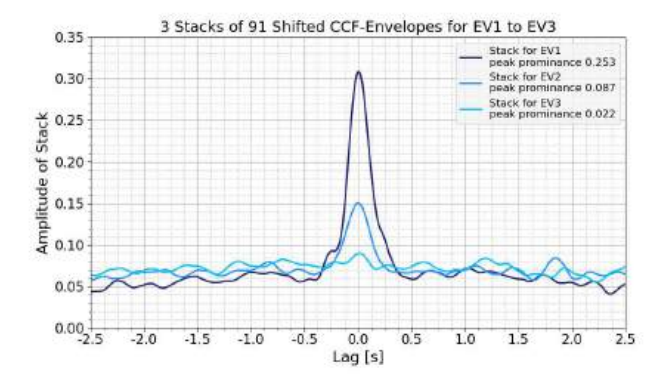


Figure 11. Stacked envelopes of CCFs between all possible combinations of stations shifted for the optimum grid point achieving the highest amplitude at 0s lag time for each of the first three EVs. The stack prominence refers to the difference between maximum and minimum stack amplitude for each EV's stack.

frequency of the Ricker wavelet is set to $13.5\ Hz$, matching the dominant tremor band we observe in the real data (see 7). These individual synthetic events are then transformed into a tremor signal by repeating the wavelet at random offsets within a certain allowed range of offsets. Afterwards, gaussian normal distributed noise is added using a standard deviation of 0.05 corresponding to half the amplitude of the maximum peak of the initial wavelet, creating a realistic poor signal to noise ratio. This is done for both sources, generating two noisy tremor signals which are filtered between 10- $20\ Hz$ and then superimposed in such a way that one tremor source becomes active slightly earlier than the other (shown in figure 10).

As described earlier, the covariance matrix may be filtered after different Eigenvectors (EVs), where the 1st EV corresponds to the most dominant source. If further sources are present in the input data, they should be recovered when filtering after the 2nd EV and so on (Soubestre et al., 2018). Since we generate synthetic tremor composed of 2 sources, we expect to recover both sources when filtering after the 1st and 2nd EV, respectively, whereas all other EVs should be carrying the uncorrelated background noise that was added to the synthetic tremor.

In figure 11 we show the stacked envelopes of the CCFs when filtering after the first three EVs for all station combinations available and time-shifted for the optimum grid point, which corresponds to the highest amplitude of the stack for all 91 station pairs. The clear peak in the stack corresponding to EV1 confirms that filtering after the 1st EV indeed retrieves the coherent signal content from one of the 2 tremor sources despite being superimposed by a second source as well as significant background noise. When filtering after the 2nd EV, a similar albeit smaller peak at zero lag time is obtained showing that the second tremor source was also well recovered. These encouraging results show that tremor source locations can be recovered, even in the case of multiple sources in close proximity, despite the poor station coverage and the challenging data conditions. As expected, when filtering after the 3rd EV, no shift of the envelopes of the CCFs for any grid point achieves a meaningful stack as there was no 3rd source active in the input data. Thus, only the uncorrelated noisy content remains and no peak in the stack of CCFs is found.

In figure 12 we show the summed up 3D likelihood functions of both synthetic tremor sources, comparing the recovered (red shapes) and true tremor source locations (corresponding green shapes). As suggested by the clear stacks found for both EVs, the two synthetic tremor sources are recovered with an accuracy of about 70 m. However, it should also be noted, how the likelihood function does exhibit some smearing around the maximum likelihood. This smearing is expected due to the stacked CCF envelope smearing as well as the high similarity in travel-times for adjacent grid points. This results in highly similar likelihood and limits the location resolution for closely spaced sources. Caution must be taken when interpreting diffusive looking likelihood functions derived from several EVs even in case of clear peaks for the stacked CCFs, as larger areas with high likelihood may be attributed to limitations in the resolution. It should also be noted, that the likelihood functions corresponding to the first 2 EVs are not weighted by their respective eigenvalues when summed up. Mathematically this assumes equally dominant tremor sources, however, the differently pronounced stacks of CCFs in figure 11 indicate that one source is more dominant than the other. In this case though, exactly weighted likelihood values are not relevant as we are interested in the distribution of the likelihood function and the position of its maximum (not the respective absolute values). Despite these constraints the successful recovery of 2 synthetic tremor sources overlain by

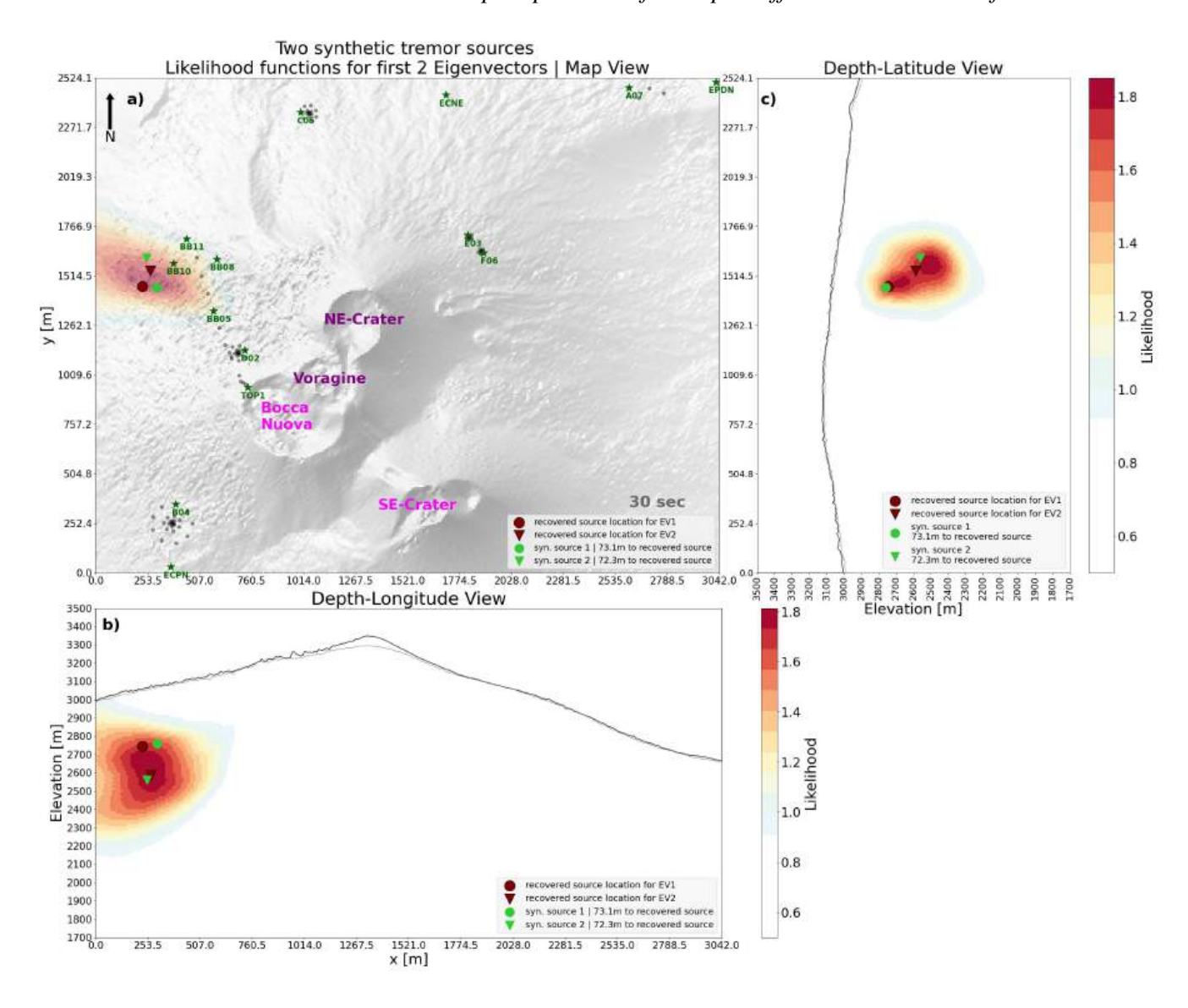


Figure 12. Likelihood function filtering after 1st and 2nd Eigenvectors (EVs) recovering both synthetic tremor sources in close proximity to one another, to the Northwest of Array D (panel a)), simulating the 300-330° source. Maximum likelihood position according to both EVs are indicated by red shapes, actual two source locations marked by corresponding green shapes. Distances of recovered source points to actual source points are given in the legend. Depth-slices cutting through the maximum likelihood positions for both EVs are plotted in panels b) and c), displaying the respective topography along both slices (black lines in panels b) and c) where the slice marking higher elevation values is slightly bolder). Stations used as input for localisation are marked as green stars, all other stations are indicated by grey dots. Note, that likelihood functions are not weighted by their respective eigenvalues when summed up.

strong random noise demonstrates how multiple individual sources are recoverable even when closely spaced. Therefore, the recovery of a larger diffusive tremor source composed of many individual sources as proposed by Bean et al. (2013) is possible when filtering after a sufficient number of EVs.

6.2 Source area recovery of high-frequency volcanic tremor from Mt. Etna

To test the 3D localisation of high-frequency volcanic tremor detected in our dataset we focus on a tremor episode between 16:00 and 17:00 UTC on 30th August, 2022, which is seen in figure 7. As illustrated, the high-frequency tremor primarily dominating the 12-15Hz band, occurs in bursts at random time intervals, with varying

durations and different intensities. Between 16:22 and 16:52 UTC clearly visible coherent signal is emerging from the background noise. This episode is one of the strongest recorded during the deployment of the array configurations while also occurring during a time of maximum station coverage. Since our station configuration is not geared towards a network-based localisation approach, we select this episode for best possible station coverage.

In figure 13 we present the respective stacks after filtering for the first 6 EVs. Each stack is computed using a total of 210 CCFs envelopes between the 21 stations selected offering the best possible station coverage, while also positioned close enough to the summit area to pick up the rapidly attenuating high-frequency range of 12-15 Hz. This corresponds to stations from Arrays E, F, B and D, as well as the linear array and the permanent INGV station ECPN. Exactly 30 minutes of data between 16:22 and 16:52 are investi-

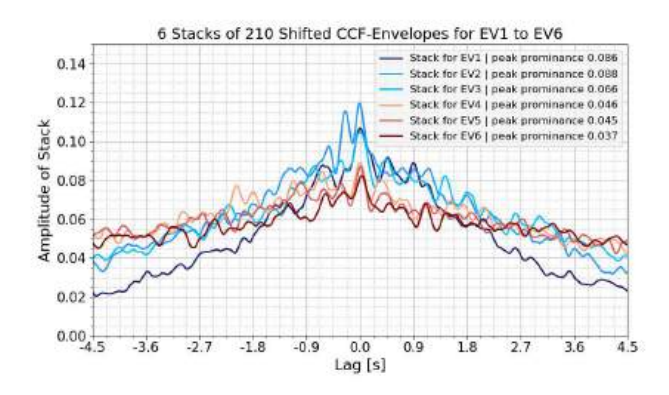


Figure 13. Stacks of Envelopes of CCFs for first 6 EVs for 210 station combinations each (21 stations) using 30 minutes of volcanic tremor as input.

gated focusing on the range between 10-20~Hz. The initial computation of the covariance matrix for the selected 21 stations is based on 45s long subwindows of which 79 consecutive windows are averaged while using an overlap of 50% resulting in one window covering the entire 30 minutes of interest. Comparing the stacks of envelopes of the CCFs obtained here 13 and those retrieved from the synthetical data 11, the stacked envelopes are clearly different now. While the shifted CCFs still create a peak at zero lag, the shape of the stacked CCFs is much flatter and the peak much less pronounced. This is indicative for a much less coherent source than the extracted synthetic tremor sources above despite the very challenging data characteristics generated for those synthetic tremors. The lower coherency showed by the real data segment may be due to the extensive wave scattering as well as rapid signal attenuation which are not included in the synthetics.

Nonetheless, we clearly recover a tremor signal here albeit less coherent or dominant within the time window, since purely uncorrelated noise would result in a completely flat stack of CCFs as observed in 11 (stack for filtering after EV3). However, the stacks corresponding to the EV 1 to 3 show an increase around zero lag time with respect to larger lag times, indicating a coherent signal emerging from the uncorrelated background noise. It is clearly noticeable, how later EVs (especially numbers 4 to 6) exhibit an increasingly flat shape suggesting that most of the coherent signal content is found on EV1 to EV3. When using the difference between largest and smallest values of each stack as a proxy for how coherent a source is, EV1 to EV2 stand out with much higher stack prominences while EV4 to EV6 are significantly flatter. EV3 is found in between. As a consequence, the high-frequency tremor detected at the time consists primarily of 2 to 3 sources, while we classify the remaining data content largely as uncorrelated background noise. The transition from a clearly identifiable source to mainly uncorrelated noise is gradual and found between EV2 (coherent signal) and EV4 (significantly larger noise dominance).

In figure 14 we show the likelihood functions corresponding to the covariance matrix decomposition into the first 3 EVs, respectively, which are then summed up. As explained in figure 12, the likelihood functions are not weighted according to the respective eigenvalues. The maximum likelihood position corresponding to EV1 is located within BNC, which is consistent with BNC being one of the main tremor source areas. The second maximum source position is found in very close proximity to Array D. Finally, the third source point is located towards the Southwest. It should be noted that the maximum likelihood for EV1 and 3 is found above the surface el-

evation that is assumed in the grid space according to Ganci et al. (2023) (see panels b) and c) in figure 14 showing the respective maximum likelihood positions above topography which are therefore plotted half transparent). We set the velocity to $1\frac{m}{a}$ for all grid points above surface elevation to force localisation below the surface, however, some high probability values are still possible above surface. It's important to clarify that we are not interested in the exact source position of a tremor signal, but interested in whether we can identify multiple individual source locations forming a tremor signal and how they roughly distribute in space. Aside from the maximum likelihood, the overall distribution for areas showing a high probability for being a source region cover mainly the regions around the summit craters as well as areas to the southwest and northwest of Array D. This is in agreement with the dominating source areas found by continuous beamforming (see section 5). For comparison, we perform beamforming for a 1-hour period covering the high-frequency tremor episode investigated between 16:22 and 16:52 UTC on 30th August, 2022, (figure 15). We lower the threshold slightly for discarding backazimuth/slowness pairs based on their respective relative power in order to achieve a more continuous evolution of both parameters over the 1-hour period. The seismic amplitudes in the top panel clearly indicate the tremor episode's appearance as the 10-minute displacement values increase significantly from 16:10 to 16:20. At that time, the previously mentioned northwestern source becomes active (between 300-330°). This signal adds to the overall seismic amplitude registered, and is anticipated to be an independent tremor source rather than originating from a reflection from the crater as disscused previously. Indeed, BNC exhibits an increase in activity at the same time suggesting inter-connected source areas if a reflection is ruled out. The third dominant source region—identified in figures 8 and 9 to the southwest, spanning approximately 210-240°—is also active during this one-hour window. However, its activity is primarily observed before 16:20 UTC and is largely absent during the 30minute interval from 16:22 to 16:52 UTC, which is the focus of the 3D grid search analysis. Nonetheless, some signal content from this direction is present. Therefore, the tremor episode in question is mainly made up of 2 sources (one within BNC and 1 to the Northwest), but a weaker third contribution from a southwestern direction may also be identified in both beamforming as well as the decomposition of the covariance matrix for EV3. Differences are noticeable though, in particular for the northwestern source appearing quite dominant in the beamforming between 300-330° while this source area is not as pronounced in figure 14.

7 NON-DEGASSING RELATED DRIVING MECHANISM OF HIGH-FREQUENCY VOLCANIC TREMOR?

Performing both multi-array beamforming as well as a 3D grid search localisation allows for insights into rarely observed high-frequency tremor's spatial distribution and, in turn, offers implications on driving mechanisms of the recorded tremor. Despite most challenging data conditions at high-frequency ranges (12-15Hz) and further limitations in terms of resolution due to a small grid space and poor azimuthal coverage, three source areas are predominantly found and 2 aspects are of particular interest. Firstly, only one of these source areas is located within the summit crater (BNC) which was continuously degassing with the corresponding tremor signals most likely linked to it. Synthetic tests as well as comparison with impulsive degassing bursts confirm a clear focus of the energy radiated from BNC, centered around the degassing vent in

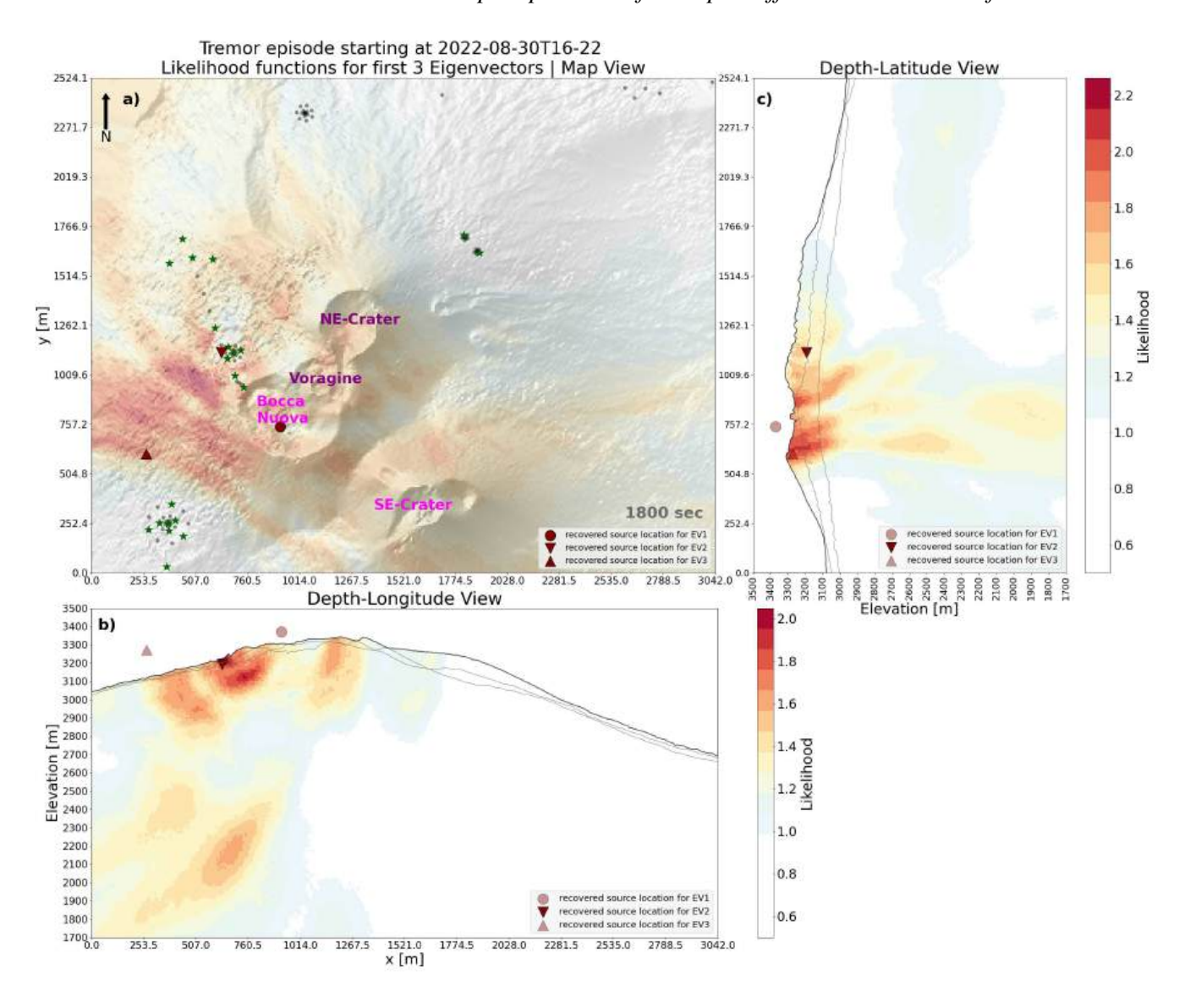


Figure 14. Likelihood functions obtained for filtering after the first 3 EVs which show a meaningful indication of a coherent signal according to the respective stacks seen in figure 13. Maximum likelihood position according to all EVs are indicated by red shapes (check legend for details including recovered source positions). As before, panel a) shows the map-view while depth-slices cutting through the maximum likelihood positions for both EVs are plotted to the right and bottom (panels b) and c)). Stations used as input for localisation are marked as green stars, all other stations are indicated by grey dots. Note that likelihood functions are not weighted by their respective eigenvalues when summed up.

BNC. Additionally, temporal variations in apparent slowness suggest changing source depths for the radiated tremor beneath BNC, as shown in figure 9. In this case, we interpret the tremor as propagating both downward and upward, completing two full cycles with a period of approximately 1.5 hours between 21:00 and 00:00 UTC on 31 August 2022. We are able to constrain impulsive degassing events' source depths to about 250 to 500m below the surface using synthetic and real apparent slownesses. Degassing as a driving force can be associated with tremor signals from this direction of arrival as previously reported by Yukutake et al. (2017)). This aligns with one of the most commonly proposed models for volcanic tremor generation, in which fluid migration plays a central role (Steinberg & Steinberg, 1975; Neuberg & Pointer, 2000; Salerno et al., 2018).

However, this model does not seem to be sufficient to explain the

other 2 tremor source areas detected, which are located off the summit crater where degassing is not expected. Instead, these source areas may be indicative of non-fluid driven processes as proposed by Bean et al. (2013) and documented through laboratory experiments by Rowley et al. (2021). We suggest that the tremor sources identified by both beamforming and 3D grid search that are located away from typical degassing sites are more likely to be driven by quasibrittle failure of the exceptionally weak material of the uppermost layers of the edifice of Mt. Etna. The rheology is largely controlled by the angle of internal frication of the material, not by its temperature. Sequences of numerous, small stress-drop, low-amplitude events merging into tremor are proposed by Bean et al. (2013) potentially purely driven by the edifice's slow deformation e.g. due to gravitational load. We suggest that tremor observed from the noncrater areas may be an example of this process. Furthermore, the

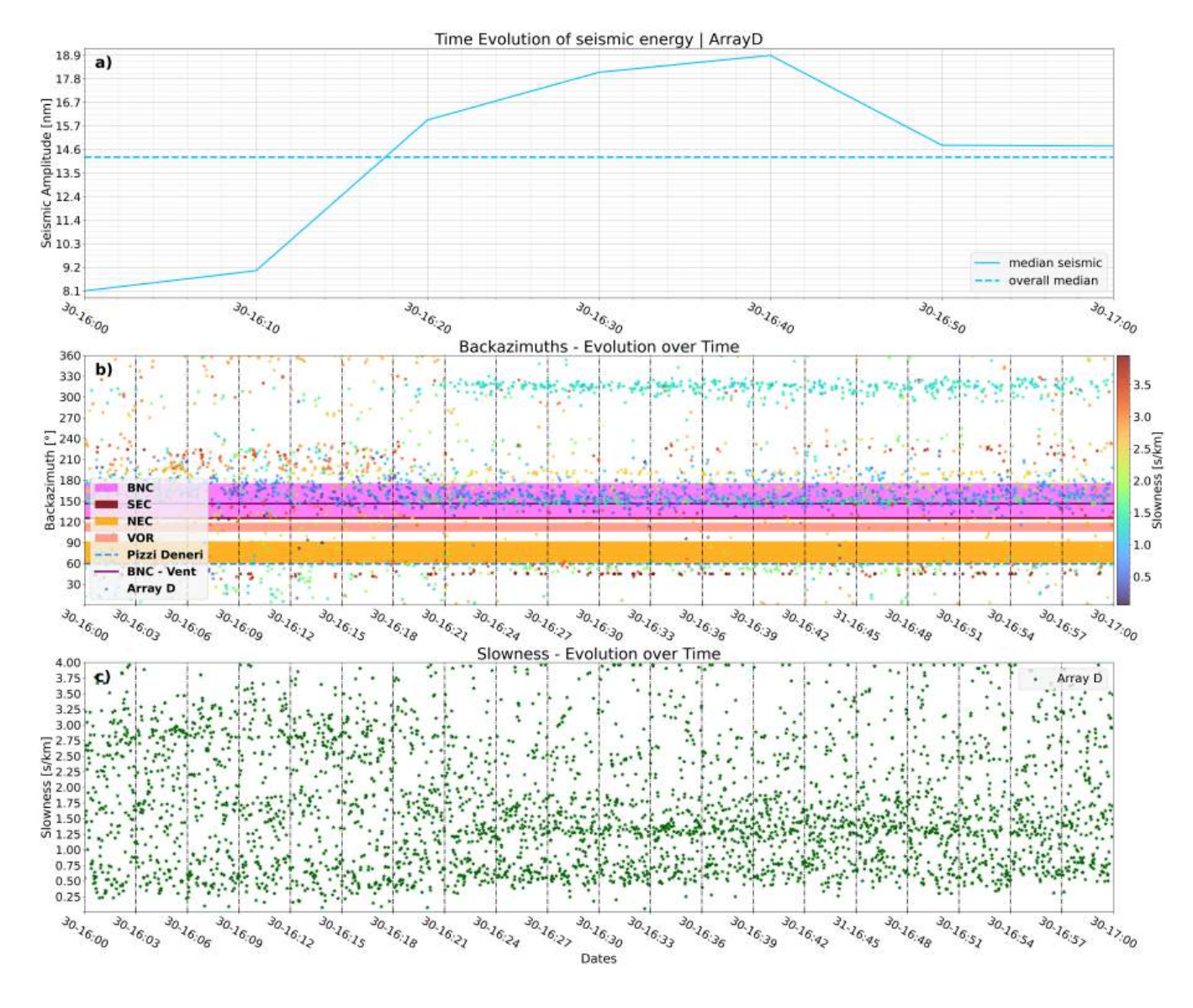


Figure 15. Beamforming targeting the tremor episode between 16:22 and 16:52 showing colour-coded backazimuth (panel b)) with respect to apparent slowness (panel c)). Median seismic amplitudes for non-overlapping 10-minute windows calculated from all stations in Array D are found in panel a).

capability of typical weak volcanic material to support seismicity despite being close to the brittle-ductile boundary has been demonstrated by Rowley et al. (2021). In fact, when increasing stress levels, tremor-train-like signals were observed very similar to those recorded on Mt. Etna.

The second significant aspect of our observations regards the spatial distribution of the recorded tremor is that the tremor sources away from the summit area do not seem to be confined to a specific location but instead are more spatially diffusive. We have conducted extensive examination of the arrays' precision and accuracy with excellent azimuthal recovery for synthetic events (e.g., at the surface at the vent's location in BNC), while showing increasing backazimuth offsets for increasing source depths as a result of 2D beamforming. Similar direction-dependent—and thus depth-dependent—variations in apparent slowness are also observed in the real data, indicating that the tremor source beneath BNC is likely confined to the vent area and is associated with vertical movement related to degassing processes. Comparing the appar-

ent slownesses for the tremor sources outside of BNC and the synthetic slownesses suggests that the slightly diffusive character of these source areas outside of BNC is a real feature rather than subject to the arrays' accuracy. It should be noted, that the source dominating the 210-240° range does also show varying apparent slownesses potentially adding to the diffusive appearance of this signal, however, these variations are smaller than what is observed for BNC. Furthermore, the apparent slownesses suggest very-near-surface sources and therefore depth-dependent variations of the corresponding backazimuth values are unlikely. In addition, the 300-330° source area shows vary stable apparent slownesses reinforcing the spatially diffusive nature of the signal. A diffusive tremor source area, however, is consistent with the diffusive damage pattern reported by and Rowley et al. (2021) as opposed to degassing-related tremor that would be more likely restricted to a certain direction of arrival pointing back to where the degassing is occurring. Instead, small-scale failure would radiate high frequencies consistent with the dominant tremor band registered.

We have shown that several individual synthetic sources may be recovered using COVSEISNET's covariance matrix decomposition (Seydoux et al., 2016; Soubestre et al., 2018) when active simultaneously and overlain by strong noise. Filtering after several EVs for a high-frequency tremor episode reveals at least 2 sources contributing to the tremor albeit coherent content is significantly less dominant than for the synthetic example. A third possible source may be considered, depending on the threshold for coherency above which data content is considered to be a tremor signal as opposed to uncorrelated background noise. Regardless, the general distribution of the likelihood functions obtained when filtering after EVs that carry meaningful signal (mainly EV1, 2 and 3 in figure 13) is in agreement with dominant directions of arrival seen with beamforming. It should be noted that the larger areas showing higher probability as potential tremor source regions should not be over-interpreted, due to the resolution limitations discussed earlier. However, the joint interpretation of both beamforming and 3D grid search suggests that diffusive tremor source areas where multiple individual sources are active are a reasonable assumption.

We also want to emphasize a possible inter-connection between these main source regions revealed through beamforming. The seismic energy output shows strong variability over time, which seems to indicate that the intensity of these sources also vary over time, and one could overshadow another. These temporal variations, characterised by appearances and disappearances of sources in our beamforming results, also appear to be correlated. Around 04:00 UTC on 26th August, 2022, (figure 8), a significant change in volcanic behaviour can be observed as seismic output subsides and both tremor sources outside of BNC cease, with only weak signals persisting from the 210-240° sector. These changes in the volcanic behaviour affect all 3 main source regions as activity in BNC is reduced as well suggesting an inter-connection between source regions. Similarly, in figure 9 the appearance of the 210-240° source coincides with BNC as well as the northwestern source area largely shutting down despite quite different seismic energy outputs in both cases around 14:00 UTC on 31st August and 07:00 UTC on 1st September. This seems to indicate not just significant temporal variations of the tremor sources but also an inter-connection between them as part of a larger complex system. Better understanding of this will require further investigations.

8 CONCLUSION

Through a large, high-resolution deployment on Mt. Etna we detect rarely observed high-frequency tremor dominating mainly in the 12-15Hz band. In case of Mt. Etna as well as most other volcanic environments such frequency ranges are often overlooked as extreme scattering and rapid attenuation only allow for recording of these signals when in very close proximity to their origin. We apply both multi-array beamforming as well as a 3D grid search based on shifted and stacked CCFs revealing three main tremor source regions across the summit. The most dominant tremor source over the course of the deployment is linked to the degassing activity at BNC. Comparison with synthetic tests allows for constraints in terms of the tremor's and impulsive degassing events' source depths, which we mainly place between elevations of about 2800 to 3000 m a.b.l. ($\sim 270-470m$ depth). Additionally, temporal variations of the apparent slownesses indicate both downward and upward propagating tremor sources beneath BNC which suggests that it is not directly fluid related. Crucially, synthetic impulsive event data demonstrates very high accuracy and precision levels in terms of the arrays localisation capabilities and a systematic offset of recovered directions of arrivals as a function of source depth.

Interestingly, there are two more source regions predominantly found which are located outside BNC, one to the southwest and one to the northwest from Array D. While the tremor located at BNC can be associated with ongoing degassing activity, this seems an unlikely driving process for those two regions outside the crater as degassing activity is not expected there. Owing to synthetic tests showing that backazimuths are accurately recovered using our station configuration as well as stable and very high apparent slownesses, we consider the spatially diffusive character of the source areas (i.e., covering ranges of $\sim 30^{\circ}$) a real feature. We suggest this characteristic is consistent with a model of numerous, small stress-drop, low-amplitude events forming a diffusive source area undergoing slow deformation. Quasi-brittle failure of the very weak material on the volcano's edifice should be considered as a possible source mechanism as it could explain the located source areas and the diffusive rather than localised appearance of this tremor. Indeed, despite a less-than-ideal station coverage, the 3D grid search localisation carried out retrieves coherent signal content for a strong tremor episode from at least two sources. Furthermore, the overall likelihood function for the tremor's source regions are largely in agreement with the dominant direction of arrival detected with beamforming, even though additional smearing can also be artificially introduced due to highly similar travel-times in the small grid space. Still, synthetic tremor simulating two individual tremor source locations embedded in significant background noise can be recovered successfully.

We thus interpret these results as an example of the variety and complexity of processes triggering volcanic tremor. While we are able to link tremor signals to the ongoing degassing activity in BNC, we also uncover tremor which may be unrelated to fluid-driven triggers due to its source locations and its diffusive characteristics. Furthermore, the temporal tracking of the high-frequency tremor with beamforming indicates a possible inter-connection of the main source areas. Changes in behaviour often seem to affect all source areas hinting at a complex system whose better understanding will require further investigations, and shows its importance to improve understanding of degassing and deformation processes in shallow areas of volcanoes.

ACKNOWLEDGMENTS

We would like to thank the IMPROVE European Horizon's 2020 research and innovation programme under Grant Agreement No. 858092 as part of which this study has been carried out as well as the SINFONIA project as part of the field campaigns to Mt. Etna. Furthermore, we would like to thank several people assisting during the huge amount of fieldwork that was conducted, in particular Vittorio Minio, Elisabeth Glueck, Regina Maass, and Eleanor Dunn.

DATA AVAILABILITY

We are in the process of uploading the seismic data used here to zenodo through which it will be accessible. The seismic data used from the INGV permanent station ECPN is freely available for download under https://eida.ingv.it/it/network/2I_2024

References

- Almendros, J., Abella, R., Mora, M. M., & Lesage, P., 2014. Array analysis of the seismic wavefield of long-period events and volcanic tremor at arenal volcano, costa rica, *Journal of Geophysical Research: Solid Earth*, 119, 5536–5559.
- Amitrano, D., 2003. Brittle-ductile transition and associated seismicity: Experimental and numerical studies and relationships with the b value, *J. Geophys. Res.*, 108, 2044-2059.
- Bean, C. J., Barros, L. D., Lokmer, I., Métaxian, J.-P., Brien, G. O., & Murphy, S., 2013. Long-period seismicity in the shallow volcanic edifice formed from slow-rupture earthquakes, *Nature Geoscience*, 7, 71-75.
- Cannata, A., Grazia, G. D., Montalto, P., Ferrari, F., Nunnari, G., Patanè, D., & Privitera, E., 2010. New insights into banded tremor from the 2008–2009 mount etna eruption, *Journal Volcanolology and Geothermal Research*, 115, B12318.
- Chardot, L., Jolly, A. D., Kennedy, B. M., Fournier, N., & Sherburn, S., 2015. Using volcanic tremor for eruption forecasting at white island volcano (whakaari), new zealand, *Journal Volcanolology and Geothermal Research*, 302, 11-23.
- Dmitrieva, K., Hotovec-Ellis, A. J., Prejean, S., & Dunham, E. M., 2013. Frictional-faulting model for harmonic tremor before redoubt volcano eruptions, *Nature Geoscience*, *6*, 652–656.
- Ganci, G., Cappello, A., & Neri, M., 2023. Data fusion for satellite-derived earth surface: The 2021 topographic map of etna volcano, *remote sensing*, 15, 198.
- Grazia, G. D., Falsaperla, S., & Langer, H., 2006. Volcanic tremor location during the 2004 mount etna lava effusion, *Geophysical Research Letters*, 33, L04304.
- Heleno, S. I., Faria, B. V., Bandomo, Z., & Fonseca, J. F., 2006. Observations of high-frequency harmonic tremor in fogo, cape verde islands, *Journal Volcanolology and Geothermal Research*, 158, Issues 3–4, 361-379.
- Ibanez, J. M., Castro-Melgar, I., Cocina, O., Zuccarello, L., Branca, S., Pezzo, E. D., & Prudencio, J., 2019. First 2-d intrinsic and scattering attenuation images of mt etna volcano and surrounding region from active seismic data, *Geophysical Journal International*, 220, 267–277.
- Konstantinou, K. I. & Schlindwein, V., 2002. Nature, wavefield properties and source mechanism of volcanic tremor: a review, Journal Volcanolology and Geothermal Research, 119, 161-187.
- Leva, C., Rümpker, G., & Wölbern, I., 2022. Multi-array analysis of volcano-seismic signals at fogo and brava, cape verde, *Solid Earth*, *13*, 1243–1258.
- Lieto, B. D., Saccorotti, G., Zuccarello, L., Rocca, M. L., & Scarpa, R., 2007. Continuous tracking of volcanic tremor at mount etna, italy, *Geophysical Journal International*, 169, 699–705.
- Lomax, A., Virieux, J., Volant, P., & Berge-Thierry, C., 2000. Probabilistic earthquake location in 3d and layered models, *Thurber C.H., Rabinowitz N. (eds) Advances in Seismic Event Location. Modern Approaches in Geophysics, Springer, Dordrecht*, 18, 101–134.
- Lomax, A., Michelini, A., & Curtis, A., 2014. Earthquake location, direct, global-search methods, *Meyers R. (eds) Encyclopedia of Complexity and Systems Science. Springer, New York, NY,* 1–33
- McNutt, S. R., 1992. Volcanic tremor, *Encyclopedia of Earth System Science*, 4.
- Neuberg, J. & Pointer, T., 2000. Effects of volcano-topography on seismic broadband waveforms., *Geophysical Journal Inter-*

- national, 101, 83-104.
- Permana, T., Nishimura, T., Nakahara, H., Fujita, E., & Ueda, H., 2019. Reliability evaluation of volcanic tremor source location determination using cross-correlation functions, *Geophysical Journal International*, 220, 1300–1315.
- Rowley, P., Benson, P. M., & Bean, C. J., 2021. Deformation-controlled long-period seismicity in low-cohesion volcanic sediments, *Nature Geoscience*, *14*, 942-948.
- Salerno, G. G., Burton, M., Grazia, G. D., Caltabiano, T., & Oppenheimer, C., 2018. Coupling between magmatic degassing and volcanic tremor in basaltic volcanisms, frontiers in Earth Science, 6, 157.
- Seydoux, L., Shapiro, N., de Rosny, J., Brenguier, F., & Landes, M., 2016. Detecting seismic activity with a covariance matrix analysis of data recorded on seismic arrays, *Geophysical Journal International*, 204, 1430-1442.
- Smith, P. & Bean, C., 2020. Retreat: A real-time tremor analysis tool for seismic arrays, with applications for volcano monitoring, *Frontiers in Earth Science, Section Volcanology, 8*.
- Soubestre, J., Shapiro, N. M., Seydoux, L., de Rosny, J., Droznin, D. V., Droznina, S. Y., Senyukov, S. L., & Gordeev, E. I., 2018. Network-based detection and classification of seismovolcanic tremors: Example from the klyuchevskoy volcanic group in kamchatka, *Journal of Geophysical Research: Solid Earth*, 123.
- Soubestre, J., Seydoux, L., Shapiro, N., De Rosny, J., Droznin, D., Droznina, S. Y., & Gordeev, E., 2019. Depth migration of seismovolcanic tremor sources below the klyuchevskoy volcanic group (kamchatka) determined from a network-based analysis, *Geophysical Research Letters*, 46 14, 8018–8030.
- Steinberg, G. S. & Steinberg, A. S., 1975. On possible causes of volcanic tremor, *Journal Geophysical Research*, 80, NO.11.
- Tong, F., Seydoux, L., Journeau, C., & Soubestre, J., 2024. Covseisnet python package, *covseisnet/covseisnet: Associate repository with a Zenodo DOI* (1.0.0) [Software]. Zenodo. doi: https://doi.org/10.5281/zenodo.10990032.
- Trovato, C., Aochi, H., & de Martin, F., 2014. Numerical modeling of seismic wave propagation on etna volcano (italy): Construction of 3d realistic velocity structures, *EGU General Assembly 2014*.
- Williams-Jones, G., Stix, J., Heiligmann, M., Barquero, J., Fernandez, E., & Gonzalez, E. D., 2001. A model of degassing and seismicity at arenal volcano, costa rica., *Journal Volcanolology and Geothermal Research*, 108, 121-139.
- Yukutake, Y., Honda, R., Harada, M., Doke, R., Saito, T., Ueno, T., Sakai, S., & Morita, Y., 2017. Analyzing the continuous volcanic tremors detected during the 2015 phreatic eruption of the hakone volcano, *Springer Open, Earth, Planets and Space, 69-164*
- Zuccarello, L., Paratore, M., Rocca, M. L., Ferrari, F., Messina, A., Branca, S., Contrafatto, D., Galluzzo, D., Rapisarda, S., & García, L., 2016. Shallow velocity model in the area of pozzo pitarrone, mt. etna, from single station, array methods and borehole data, ANNALS OF GEOPHYSICS, 59, 4.
- Zuccarello, L., Angelis, S. D., Minio, V., Saccorotti, G., Bean, C. J., Paratore, M., & Ibanez, J. M., 2022. Volcanic tremor tracks changes in multi-vent activity at mt. etna, italy: Evidence from analyses of seismic array data, *Geophysical Research Letters*, 49, 22.